ELSEVIER

Contents lists available at ScienceDirect

# Science Bulletin

journal homepage: www.elsevier.com/locate/scib



# Article

# Coping with the concurrent heatwaves and ozone extremes in China under a warming climate

Mengmeng Li <sup>a,b</sup>, Xin Huang <sup>a,b,\*</sup>, Dan Yan <sup>a</sup>, Shiyi Lai <sup>a</sup>, Zihan Zhang <sup>a</sup>, Lei Zhu <sup>c,d</sup>, Yuting Lu <sup>a</sup>, Xinyi Jiang <sup>a</sup>, Nan Wang <sup>e</sup>, Tijian Wang <sup>a</sup>, Yu Song <sup>f</sup>, Aijun Ding <sup>a</sup>

- <sup>a</sup> School of Atmospheric Sciences, Nanjing University, Nanjing 210023, China
- <sup>b</sup> Frontiers Science Center for Critical Earth Material Cycling, Nanjing 210023, China
- <sup>c</sup> School of Environmental Science and Engineering, Southern University of Science and Technology, Shenzhen 518055, China
- d Guangdong Provincial Observation and Research Station for Coastal Atmosphere and Climate of the Greater Bay Area, Shenzhen 518055, China
- <sup>e</sup> College of Carbon Neutrality Future Technology, Sichuan University, Chengdu 610044, China
- <sup>f</sup>Department of Environmental Science, Peking University, Beijing 100871, China

#### ARTICLE INFO

#### Article history: Received 20 October 2023 Received in revised form 22 March 2024 Accepted 25 March 2024 Available online 25 May 2024

Keywords:
Heatwave
Ozone
Biogenic emission
Dry deposition
Ozone-temperature sensitivity

#### ABSTRACT

Intensive human activity has brought about unprecedented climate and environmental crises, in which concurrent heatwaves and ozone extremes pose the most serious threats. However, a limited understanding of the comprehensive mechanism hinders our ability to mitigate such compound events, especially in densely populated regions like China. Here, based on field observations and climate-chemistry coupled modelling, we elucidate the linkage between human activities and the climate system in heatrelated ozone pollution. In China, we have observed that both the frequency and intensity of heatwaves have almost tripled since the beginning of this century. Moreover, these heatwaves are becoming more common in urban clusters with serious ozone pollution. Persistent heatwaves during the extremely hot and dry summers of 2013 and 2022 accelerated photochemical ozone production by boosting anthropogenic and biogenic emissions, and aggravated ozone accumulation by suppressing dry deposition due to water-stressed vegetation, leading to a more than 30% increase in ozone pollution in China's urban areas. The sensitivity of ozone to heat is demonstrated to be substantially modulated by anthropogenic emissions, and China's clean air policy may have altered the relationship between ozone and temperature. Climate model projections further highlight that the high-emission climate-socioeconomic scenario tends to intensify the concurrent heat and ozone extremes in the next century. Our results underscore that the implementation of a strict emission strategy will significantly reduce the co-occurrence of heatwaves and ozone extremes, achieving climate and environmental co-benefits.

© 2024 Science China Press. Published by Elsevier B.V. and Science China Press. All rights are reserved, including those for text and data mining, Al training, and similar technologies.

# 1. Introduction

Human activity, with accelerated urbanization, has brought about unprecedented climate and environmental crises in global cities. Under a warming climate and local urban influence, heatwaves (typically defined as persistent high air temperatures above the mean climate state) have frequently scorched many regions across the world [1]. The increasingly frequent and prolonged heat extremes have caused disastrous threats, such as excess heat-related mortality and economic damages [2]. In addition, tropospheric ozone (O<sub>3</sub>) is the primary air pollution concern in urban areas, and its levels tend to soar during heatwaves [3,4]. Such co-

E-mail address: xinhuang@nju.edu.cn (X. Huang).

occurrence of heatwaves and ozone extremes could pose a particularly serious threat to human health and has become the main public hazard in global cities [5].

Tropospheric  $O_3$  is predominantly formed by the photochemical reactions of nitrogen oxides  $(NO_x)$  and volatile organic compounds (VOC). Deteriorated ozone pollution during heatwaves involves complex interactions among atmospheric physical and chemical processes. During heat extremes, the significantly higher air temperature could accelerate  $O_3$  production by 2–8 ppbv/°C in major cities worldwide by hastening the chemical reaction rate and thermal decomposition of peroxyacetyl nitrate (PAN) [6–8]. Besides, the intense incident solar radiation, dry and stagnant atmosphere typically associated with hot periods also exacerbate the accumulation of  $O_3$  near the surface [9,10]. Such a positive  $O_3$  anomaly could also be greatly enhanced by the advection and vertical

<sup>\*</sup> Corresponding author.

mixing that entrains high- $O_3$  air masses downwind due to persistent high-pressure systems, such as, the 2003 European heatwave [3].

Despite the advances in understanding the comprehensive mechanisms of heat-related ozone pollution, it remains challenging to elucidate the complex interactions among human and natural systems in such compound events. Vegetation and human responses to heat complicate this compound heatwave and ozone extreme [11]. Evidence from field campaigns and model simulations indicates that biogenic volatile organic compound (BVOC) emissions from vegetation could be significantly enhanced or suppressed during extreme heatwaves [12,13] and accompanying drought conditions [14]. The increased biogenic emissions and accelerated photochemical reactions due to warmer air temperatures could explain the unusually high levels of O<sub>3</sub> observed during heatwaves in European [12.15] and Chinese megacities [13]. However, some studies have also observed a suppression of ozone formation at extremely high temperatures due to chemical and biophysical feedbacks [7,16]. Meanwhile, considering that dry deposition is an important sink for ozone, a decrease in the stomatal uptake of O<sub>3</sub> by water-stressed vegetation (a key element of dry deposition) could worsen ozone pollution during periods of extreme heat [17].

Anthropogenic emissions, along with heat-induced emission changes, may further exacerbate ozone pollution during extreme heat events. The relationship between ozone and temperature is highly dependent on the ambient  $NO_x/VOC$  ratio [6,18]. The abundance of  $NO_x$  in the atmosphere, primarily released by human activities such as fossil fuel combustion, has changed dramatically in recent years in highly industrialized regions like China [19]. This change would significantly affect the sensitivity of  $O_3$  to air temperature. Urban energy consumption, such as the use of air conditioning, and evaporative emissions also tend to increase under sustained high temperatures [20]. Therefore, heat-related ozone pollution is far more complicated in these emission-intensive regions. However, our understanding of the complex response of ozone to heat and the role of human activities is still limited.

With a faster warming rate than the global average (e.g., 0.26 vs.  $0.15 \,^{\circ}\mathrm{C} \, (10 \,^{\circ}\mathrm{a})^{-1}$  for the annual average air temperature between 1951 and 2021) [21], China has become one of the most vulnerable regions to frequent climatic disasters worldwide. Over the past 20 years, China has experienced its warmest period on record, with a notable increase in extreme heat events, for instance, the exceptionally hot and dry summers in 2013 and 2022. China is simultaneously the most populous and economically dynamic country in the world. It is experiencing deteriorated ozone pollution, which is even worse than in any other region worldwide [22,23]. Under global climate warming, summertime heatwaves are projected to become more intense, more frequent, and longer-lasting [24]. The projected warmer summers pose a new challenge to the survival of city residents, highlighting the great importance of a comprehensive understanding of mechanisms and mitigation strategies for heat-related air pollution in Chinese megacities.

# 2. Materials and methods

# 2.1. Data

Global reanalysis data. We utilize the fifth-generation European Centre for Medium-Range Weather Forecasts (ECMWF) reanalysis data (ERA5; https://www.ecmwf.int) for global climate analyses [25]. The ERA5 reanalysis data are at a spatial resolution of  $0.25^{\circ} \times 0.25^{\circ}$  and a temporal resolution of 1 h. Hourly 2-m air temperature data for June to August from 1961 to 2022, focusing on the East Asia region ( $10^{\circ}$ - $60^{\circ}$ N,  $70^{\circ}$ - $140^{\circ}$ E), are utilized to calculate the daily maximum air temperature ( $T_{max}$ ) and analyze the

trends of heat extremes. Total precipitation (TP) is used to calculate the precipitation anomaly for the same 53-year period. Other meteorological variables include surface pressure, dew point temperature, zonal wind, meridional wind, boundary layer height, and ultraviolet radiation for June–August from 2013 to 2022 to demonstrate the impacts of air pollution meteorology on heatdays and non-heatdays.

Ground-level ozone data. Real-time ozone levels are regularly monitored and reported by the Ministry of Ecology and Environment in China (MEE; https://www.mee.gov.cn). The national air quality monitoring network was launched in 2013 as part of China's Clean Air Action Plan and included 450 monitoring stations in 74 major cities. It has now grown to more than 1,500 stations in 454 cities across China. In this study, the maximum daily 8-h average (MDA8) O<sub>3</sub> concentrations for June–August of 2013–2022 were downloaded from https://quotsoft.net/air, a mirror of the MEE official platform, and calibrated to analyze the regional ozone pollution in China.

Satellite formaldehyde (HCHO) column density. Tropospheric HCHO column density, measured daily at a resolution of 7 km  $\times$  3.5 km by the Tropospheric Monitoring Instrument (TRO-POMI) onboard the Sentinel-5P satellite since 2018 [26], is used for model comparison. The overpass time for TROPOMI is around 13:30 local time, so model results are sampled at that time. The satellite data can be freely accessed from the National Aeronautics and Space Administration (NASA) Goddard Space Flight Center at https://acd-ext.gsfc.nasa.gov.

Air pollution campaigns and instruments. An air pollution campaign was conducted at the Station for Observing Regional Processes of Earth System (SORPES) at Nanjing University. The station is located in the northeast of downtown Nanjing (32.12°N, 118.95°E) and serves as a background site of the Yangtze River Delta [27]. Trace gases, including O<sub>3</sub>, nitrogen dioxide (NO<sub>2</sub>), and VOC have been measured at SORPES since 2011. The TEI 42i was coupled with a highly selective photolytic converter to measure NO<sub>2</sub>. Real-time VOC were measured using GC-MS/FID to determine the ambient VOC concentrations with a time resolution of 1 h. Instruments were automatically span- and zero-checked and manually calibrated once a week. In this study, the ambient concentrations of NO2 and several VOC species measured at SORPES, along with local air temperatures extracted from ERA5 reanalysis data during June-August 2022, are utilized to demonstrate the responses of biogenic and anthropogenic emissions to

Emissions from coal-fired power plants.  $NO_x$  emissions from coal-fired power plants across China are accessible through the Professional Knowledge Service System for Energy (energy.qibebt.ac.cn/index, Power plant emissions of  $NO_x$  (2017–2019)). In this study, the monthly  $NO_x$  emissions and local air temperatures recorded at 47 coal-fired power plants in the urban agglomerations of eastern China, including Shanghai (2), Jiangsu (32), Anhui (10), and Zhejiang (3) over June–August in 2017–2019, are utilized to illustrate the responses of power plant emissions to extreme heat conditions. Monthly power generation capacities reported by the National Bureau of Statistics of China (https://data.stats.gov.cn/) are also supplemented to illustrate the surging urban electricity demand during prolonged periods of high air temperatures.

Global climate model projections. CMIP6 is the latest version of the Coupled Model Intercomparison Project (CMIP) organized by the World Climate Research Program (WCRP; https://wcrp-cmip.org/cmip-phase-6-cmip6). CMIP6 produces global climate projections by integrating different Shared Socioeconomic Pathways (SSPs) and Representative Concentration Pathways (RCPs). There are a total of five SSP pathways ranging from sustainable development (SSP1) and middle-of-the-road development (SSP2) to high inequality between countries (SSP3 and SSP4) and fossil-fueled

development (SSP5). When a specific radiation forcing (RF) target (e.g., 2.6 W m<sup>-2</sup> in 2100 under RCP2.6) is imposed as a constraint on the SSP pathway (e.g., SSP1 and SSP2, labeled as SSP126 and SSP226), the carbon emissions are adjusted to meet the RF level.

In this study, we obtained the essential climate model forecasts, including daily maximum air temperature and average NO<sub>2</sub> concentrations, from the CMIP6 archive under five SSP-RCP scenarios for the future period of 2015–2100. These five SSP-RCP scenarios include SSP119 (sustained development with RF of 1.9 W m<sup>-2</sup> to limit the warming level below 1.5°C), SSP126 (sustained development with RF of 2.6 W m<sup>-2</sup> to limit the warming level below 2.0°C), SSP245 (middle development with RF of 4.5 W m<sup>-2</sup>), SSP370 (medium-to-high emissions with RF of 7.0 W m<sup>-2</sup>), SSP585 (high-emission scenario with RF of 8.5 W m<sup>-2</sup>). Considering the availability of all required variables and scenarios, three global climate models (GCMs: Table 1) are selected.

#### 2.2. Definition of heatwave and its cumulative intensity

So far, there is no universal definition for a heatwave. Here we define a heatwave based on the critical threshold method that has been extensively used in the literature [1,28]. The day with a daily maximum air temperature exceeding the 90th percentile of the temperature distribution (T<sub>max\_90th</sub>) based on a centered 15-d window during 1961–1990 ( $T_{\text{max}} \ge T_{\text{max}\_90\text{th}}$ ) is defined as a heatday. We define a heatwave event as at least 3 consecutive days with temperatures exceeding the specific threshold. Heatwave frequency is defined as the total number of days experiencing heatwaves. Apart from the frequency of heatwaves, we are also interested in the cumulative intensity of heatwaves (HCI), which refers to the total excess heat above the temperature threshold for all the heatwave days. Heatwave cumulative intensity is a measure that combines the intensity, duration, and spatial extent of a heatwave event. When referring to the cumulative intensity of a heatwave in a specific region, we calculate the average heat exceedance for all land grid points as shown in Eq. (1).

$$HCI = \sum_{1}^{N} \sum_{1}^{d} (T_{\text{max}} - T_{\text{max}\_90\text{th}})/N, \tag{1}$$

where N is the number of land grid points for each region; d is the number of consecutive heatwave days;  $T_{\rm max}$  is the daily maximum air temperature;  $T_{\rm max\_90th}$  is the 90th percentile of the daily maximum air temperature distribution during the base period.

# 2.3. Regional climate-chemistry model simulation

We use the Weather Research and Forecasting/Chemistry (WRF/Chem) model version 4.1 [29] to simulate the concurrent heatwave and ozone events in China. The modelling domain is configured with a grid of  $211 \times 182$  at a 25 km horizontal resolution, covering China's mainland. 6-h,  $0.25^{\circ} \times 0.25^{\circ}$  ERA5 reanalysis data are regularly used as the initial and lateral boundary meteorologi-

**Table 1**Basic information for the 3 GCMs from CMIP6 used in this study.

CMIP6 model	Institution	Horizontal resolution (latitude × longitude)
GFDL-ESM4	Geophysical Fluid Dynamics Laboratory, Princeton, USA	1°×1.25°
MRI-ESM2-0	Meteorological Research Institute, Tsukuba, Japan	1.125°×1.125°
UKESM1-0-LL	Met Office Hadley Center	1.25°×1.875°

cal conditions. The land surface process is represented by the Noah-Multi-parameterization (Noah-MP) model, which includes a dynamic vegetation module to simulate plant photosynthesis and stomatal conductance, carbon partitioning, and plant growth [30]. Gas-phase chemistry is simulated using the Carbon Bond Mechanism version Z (CBMZ) module [31]. Anthropogenic emissions adopt the  $0.25^{\circ}$  Multi-resolution Emission Inventory model for Climate and air pollution research (MEIC; http://meicmodel.org) from 2013 to 2020, developed by Tsinghua University. BVOC [32,33] and soil  $NO_x$  [34] emissions are calculated online using the Model of Emissions of Gases and Aerosols from Nature (MEGAN) version 2.04 as Eq. (2).

$$E_{\text{BVOC}} = \text{EF} \times \gamma_{\text{T}} \times [(1 - \text{LDF}) + \text{LDF} \times \gamma_{\text{P}}] \times \gamma_{\text{LAI}} \times \gamma_{\text{age}} \times \gamma_{\text{SM}},$$
  

$$E_{\text{NO}_{\text{Y}}} = \text{EF} \times \exp(0.071 \times T_{\text{s}}),$$
(2)

where  $E_{\rm BVOC}$  represents the BVOC emission flux under real atmospheric conditions;  $E_{\rm NO_x}$  stands for the soil  ${\rm NO_x}$  emission flux under real atmospheric conditions; EF denotes the canopy-scale emission factor under standard conditions; and LDF refers to the light-dependent function. Deviations of BVOC emissions from the standard conditions are adjusted using a set of activity factors for air temperature ( $\gamma_{\rm T}$ ), photosynthetically active radiation ( $\gamma_{\rm P}$ ), biomass density ( $\gamma_{\rm LAI}$ ), leaf development ( $\gamma_{\rm age}$ ), and soil moisture ( $\gamma_{\rm SM}$ ). For  ${\rm NO_x}$  emissions from the natural soil nitrogen pool, only the impacts of soil temperature ( $T_{\rm S}$ ) are considered.

In the WRF/Chem model, the ozone dry deposition velocity ( $v_{\rm d}$ ) is parameterized using the resistance-in-series dry deposition scheme as described in Wesely [35].

$$v_{\rm d} = (R_{\rm a} + R_{\rm b} + R_{\rm c})^{-1},$$
 (3)

where  $R_a$  represents the aerodynamic resistance;  $R_b$  stands for the laminar layer resistance;  $R_c$  denotes the surface resistance, as expressed in Eq. (4).

$$\frac{1}{R_c} = \frac{1}{R_s + R_m} + \frac{1}{R_{lu}} + \frac{1}{R_{cl}} + \frac{1}{R_g},\tag{4}$$

where  $R_s$  is the canopy stomatal resistance calculated using an empirical algorithm dependent on solar radiation and temperature (Eq. (5));  $R_m$  is the mesophyll resistance;  $R_{lu}$  is the skin resistance;  $R_{cl}$  is the lower canopy resistance;  $R_g$  is the ground resistance.

$$R_s = r_m \times (1 + (200 \times (G + 0.1)^{-1})^2) \times (400 \times (T \times (40 - T))^{-1}) \times \frac{D_{\text{H}_2\text{O}}}{D_{\text{O}_3}}, \tag{5}$$

where G represents solar radiation; T stands for the surface air temperature;  $r_{\rm m}$  is the minimum stomatal conductance dependent on vegetation type and season;  $D_{\rm H_2O}$  and  $D_{\rm O_3}$  represent the molecular diffusivity for vapor and ozone, respectively.

However, the Wesely [35] scheme does not explicitly account for the impact of soil drying on stomatal closure and fails to accurately reflect  $O_3$  deposition under extreme hot and drought conditions. Instead, we replace the canopy stomatal resistance in the Wesely scheme with that calculated from the Noah-MP dynamic vegetation module, as validated by Jin et al. [36]. Leaf-scale stomatal resistance ( $\gamma_s$ ) and dynamic leaf area index (LAI) calculated using the Farquhar/Ball-Berry model in Noah-MP are integrated to derive the canopy stomatal resistance (Eq. (6)). The Noah-MP canopy stomatal resistance is then used to calculate the gas dry deposition velocity.

$$\frac{1}{r_{s}} = b + m \times A_{n} \times h_{s}/c_{s},$$

$$\frac{1}{R_{s}} = \frac{f_{sun} \times LAI}{r_{s}^{sun}} + \frac{(1 - f_{sun}) \times LAI}{r_{s}^{sha}},$$
(6)

where  $r_{\rm s}$  is the leaf-level stomatal resistance;  $A_{\rm n}$  is the carbon assimilation rate limited by air temperature and soil moisture; b is the minimum stomatal conductance; m is the slope of the conductance-photosynthesis relationship;  $h_{\rm s}$  is the fractional humidity at the leaf surface;  $c_{\rm s}$  is the CO<sub>2</sub> concentration at the leaf surface; LAI is the dynamic leaf area index dependent on plant photosynthesis and respiration;  $f_{\rm sun}$  is the fraction of sunlit leaf;  $r_{\rm s}^{\rm sun}$  and  $r_{\rm s}^{\rm sha}$  are the leaf-scale stomatal resistance for sunlit and shaded leaves.

Here, we conduct multiple regional meteorology-chemistry coupled simulations with process diagnosis to elucidate the underlying mechanisms contributing to exacerbated ozone pollution during heat extremes. The *Base* simulation is designed with fixed anthropogenic and biogenic emissions at a specific year as input to WRF-Chem. The *NoBio* simulation is designed with biogenic emissions turned off in the model. The *Power* simulation is designed with anthropogenic emissions from coal-fired power plants, which is assumed to increase by 30% during heatwaves in the severely affected regions (see Section 3.2). These sensitivity simulations lasted from May to August in 2013 and 2022, with the first month designated as a spin-up period.

### 2.4. Photochemical box model simulation

To determine the ozone-temperature relationships under varying NO<sub>x</sub> and VOC conditions, we conducted a series of idealized simulations using a photochemistry box model coupled with the CBMZ gas-phase chemical mechanism [31]. We designed a matrix scenario that maintains the initial concentrations of VOC constant at 30 ppbv, which is a typical value in Chinese cities [37]. The air temperature ranges from 31 to 41 °C (in increments of 0.5 °C), which is typical for China's summertime heatwave. The initial concentrations of NO<sub>x</sub> range from 5 to 60 ppbv, increasing in increments of 5 ppbv at each temperature step. The O<sub>3</sub>-NO<sub>x</sub>temperature scenarios are repeated with temperature-dependent and temperature-independent isoprene emissions to determine the roles of increased BVOC emissions and chemical reaction rates in the O<sub>3</sub>-NO<sub>2</sub>-temperature relationship. Another set of O<sub>3</sub>-VOCtemperature scenarios is designed to determine the relationships between O<sub>3</sub>, VOC, and temperature, with initial NO<sub>x</sub> concentrations fixed at 30 ppbv and varying VOC concentrations (10-50 ppbv) and air temperature (31-41 °C). Also, the temperature-dependent isoprene emissions are considered in all the O<sub>3</sub>-VOC-temperature scenarios. This range of NO<sub>x</sub> and VOC mixing ratios covers the air pollution conditions in clean and urban regions. The initial concentrations of other air pollutants are obtained from the WRF-Chem model results.

# 3. Results

# 3.1. Escalating ozone pollution with intensifying heatwaves in China

Heatwaves have been intensifying in the mid-latitude Northern Hemisphere as the climate warms [1]. China has frequently experienced hot summers in recent years and was recently affected by its most severe one ever recorded in the summer of 2022. Here, we analyze the trends of heatwave frequency and intensity over China during the summer season (June–August) from 1961 to 2022 using ERA5 reanalysis data (Fig. 1a). Both heatwave metrics show similar accelerated trends since the beginning of this century, coinciding with the onset of rapid industrialization and urbanization in China. The frequency of heatwaves has increased by 2.2 d per decade since 2000, constituting 2–3 times the historical trend (0.8 d (10 a)<sup>-1</sup> between 1961 and 2000). In terms of heatwave cumulative intensity, the increasing trend is even more pronounced, at 3.9 °C per decade since 2000, more than tripling

the warming trend observed in 1961–2000. In the recent ten years, the frequency and intensity of heatwaves have increased to  $10.5~\rm d~a^{-1}$  and  $18.4~\rm ^{\circ}C~a^{-1}$  in China, nearly three to four times higher than those in the past six decades, and they incline to be increasingly concentrated in the densely populated metropolitan areas of mid-eastern China (Fig. S1 online). Such an intensified heatwave trend has been linked to the accelerated climate warming caused by greenhouse gas emissions [38] and local urban expansion [24].

The nationwide observations of surface O<sub>3</sub> at thousands of monitoring stations across China, which have been routinely recorded for the past decade (2013-2022), indicate more severe ozone pollution during heatwaves than on non-heatdays. As illustrated in Fig. S2 (online), China is currently facing severe ozone pollution, with a hotspot in the highly industrialized metropolitan areas. The summer-mean MDA8 O<sub>3</sub> concentrations have already exceeded the World Health Organization's guideline of 100 ug m across China. And it gets even worse during heatwaves, which is manifested as a notable upward shift in the probability distribution of MDA8 O<sub>3</sub> concentrations (Fig. 1a). The probability of MDA8 O<sub>3</sub> exceedance may increase from 62.4% on non-heatdays to 82.5% on heatdays. Quantitatively, the unusually high air temperature on heatdays tends to result in a positive ozone anomaly exceeding  $30\ \mu g\ m^{-3}$  in metropolitan areas compared with the non-heatdays, along with a 29.3% increase in the national average MDA8 O<sub>3</sub> concentration (Fig. S2 online).

It is worth noting that, in spatial terms, the intensifying heatwaves tend to concentrate in the middle and lower reaches of the Yangtze River and their adjacent regions (enclosed area in Fig. S3 online, hereafter referred to as the "YR region"), where both population density (Fig. 1b) and vegetation coverage are particularly high. As shown in Fig. S3 (online), 2013 and 2022 marked exceptionally hot and dry summers, with the majority of the YR region experiencing persistent high air temperatures and precipitation anomalies (Figs. S3, S4 online). The scope and intensity of the two hot summers fall outside the ranges of any extreme episodes ever recorded in China, leading to thousands of heatrelated illnesses [39]. Worse still, the Yangtze River Delta (YRD) region, located on the eastern coast, is China's largest economic zone and a fast-growing metropolitan area that is home to 16% of the national population. Huge emissions of air pollutants due to rapid urbanization have led to deteriorated O<sub>3</sub> pollution in this region, and it is worsening despite strict emission controls implemented in the past decade [22]. The abnormally enhanced ozone and sustained high temperatures frequently co-occur for more than 15 d  $a^{-1}$  (defined as the sum of days with both  $T_{\text{max}}$  and MDA8 O<sub>3</sub> exceedances) in this region (Fig. 1b), posing a significant threat to the survival of urban dwellers.

# 3.2. Anthropogenic and biogenic emission responses to heatwaves

The exacerbated ozone pollution during a heatwave is not only associated with the high air temperature that directly accelerates ozone photochemistry but also with the heat-related precursor emissions that fuel ozone formation. The temperature-dependent BVOC emission, a major precursor with a high potential for ozone formation, has already been identified in laboratory studies [40,41]. Based on the meteorology-dependent BVOC emissions estimated by the state-of-the-art biogenic emission algorithm MEGAN [32], we find a significant increase in BVOC emissions (defined as the sum of isoprene, monoterpenes, and sesquiterpenes) on heatdays, particularly in the densely vegetated regions of eastern and southern China (Fig. 2a). The total BVOC emission is estimated to be 792.7 ± 163.7 and 796.8 ± 185.0 Mmol d<sup>-1</sup> over the severely affected YR region on heatdays in the extremely hot summers of 2013 and 2022, nearly two times that of non-heatdays

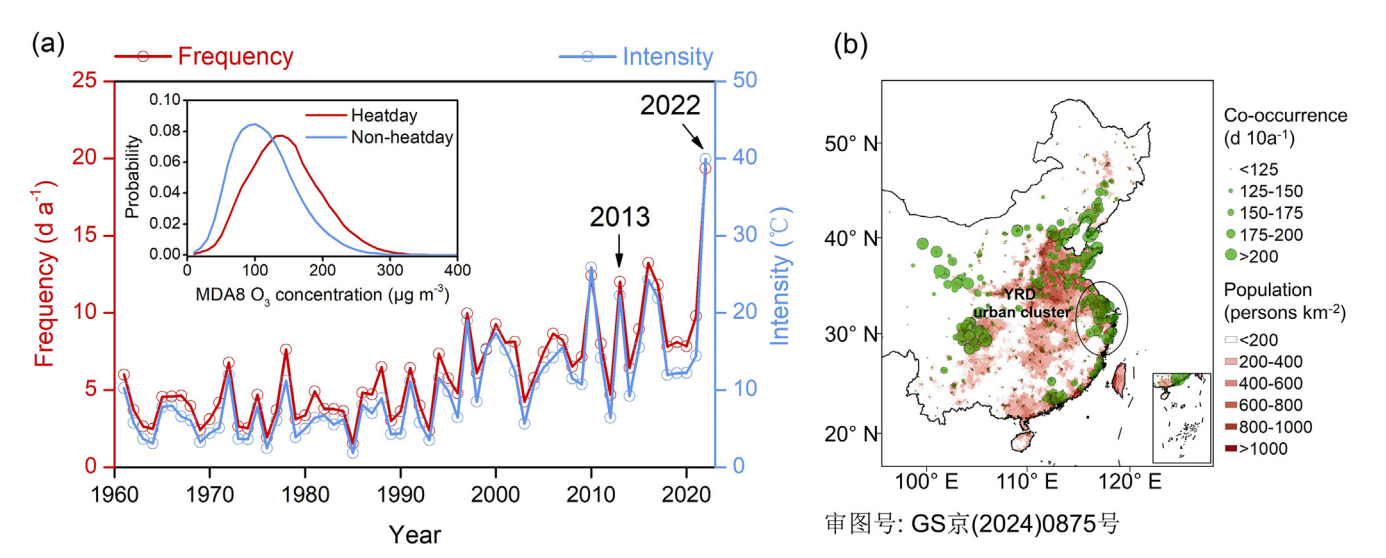


**Fig. 1.** Exacerbated summertime ozone pollution in China as the climate warms. (a) Increasing frequency and intensity of heatwaves during June–August from 1961 to 2022 in China. Probability distribution of MDA8 O<sub>3</sub> concentrations for heatdays and non-heatdays during 2013–2022 is also inserted in (a). (b) Co-occurrence frequency of heatwave and O<sub>3</sub> extremes at China's air quality monitoring network during June–August from 2013 to 2022. The shaded area in (b) represents the population density.

(Fig. 2b). Further justification comes from the inter-annual variations of satellite-observed and simulated tropospheric HCHO densities in China, a high-yield product of VOC oxidation widely used to track the BVOC emission (Fig. S5 online) [42.43]. The WRF/Chem model effectively captures the spatio-temporal behaviors of HCHO columns, although with a moderate positive bias of ~20%. Overprediction of satellite HCHO columns has been commonly reported in regional models using MEGAN, which may be related to systematic biases in BVOC emission factors and isoprene reaction schemes [44-47]. The seasonal mean HCHO densities retrieved from both satellite observations and model simulations show a clear interannual variation and reach a peak in several typical heatwave years (e.g., 2013 and 2022), indicating enhanced biogenic emissions due to high temperatures. Some studies have also highlighted that NO<sub>x</sub> emissions from the natural soil nitrogen pool and fertilizer use could significantly impact O<sub>3</sub> pollution in intensive agricultural regions [47,48]. Using the simple soil NO<sub>x</sub> emission algorithm in MEGAN, it is estimated that soil NO<sub>x</sub> emissions only contribute 5%–7% to anthropogenic NO<sub>x</sub> sources in central-eastern China, even with a 50% increase during heatwave conditions. It should be noted that the simplified parameterization and neglect of fertilizerinduced soil NO<sub>x</sub> emissions in MEGAN may underestimate the soil  $NO_x$  emissions and their contribution to  $O_3$  pollution [47,48].

In addition, the field measurements of VOC concentrations at SORPES, situated northwest of the YRD urban agglomeration and most affected by heat extremes, reveal a nearly two-thirds increase in the daily maximum isoprene concentration from 1.8 ppbv on non-heatdays to 2.9 ppbv on heatdays in June-August 2022 (Fig. 2b). The simultaneous observations of ambient isoprene concentrations and local air temperature at SORPES indicate a statistically positive isoprene-temperature dependence. There is a dramatic increase in isoprene concentration at 0.24 ppbv/°C over the 20-40 °C temperature range (Fig. S6 online), consistent with field campaigns during the 2003 European heatwave [49]. We also compare the ground-level measurement of isoprene at SORPES with WRF/Chem predictions (Fig. S7 online). It is found that the WRF/Chem model could reproduce the observed concentrations of isoprene, averaging 2.2 ppbv for simulation compared to 2.4 ppbv for observation. The model also captures the strong temperature-dependence of isoprene at 0.26 ppbv/°C, as well as the significantly increased isoprene simulated during hightemperature periods.

Heat stress may also lead to disruptions in human activities and the resulting anthropogenic emissions from megacities [50]. Unlike the soaring BVOC emissions, we observe a negligible decrease in the concentration of benzene (a marker species of anthropogenic VOC) at SORPES (Fig. S6 online). This indicates that the enhanced evaporative VOC emission under high air temperature is not significant in this situation. In addition, using 3-year statistical data on NO<sub>x</sub> emissions from 47 individual thermal power plants in the YRD urban agglomeration (energy.qibebt.ac.cn/index, Power plant emissions of  $NO_x$  (2017–2019)), we observe a rise in  $NO_x$  emissions from power plants with a positive temperature anomaly by approximately 3.8%/°C. Consequently, there is a 21.9% higher  $NO_x$ emission on heatdays compared with non-heatdays (Fig. S8 online). The increased power plant emissions might be driven by the surging urban electricity demand during sustained high temperatures. For example, the coal-fired power generation capacity in the YR region increased by 12.7% in the summer of 2013 and 11.5% in the summer of 2022 compared with the previous year. Using satellite measurements and inverse modelling, Liu et al. [51] also noted that the satellite NO<sub>2</sub> column over thermal power plants in China and India was enhanced by 4.1%-23.7% during heatwaves. They attributed such spiked emissions to the heatinduced increase in electricity use and demonstrated that the bottom-up inventory underestimated the emissions from the power sector by 34.9% for the selected heatwave event. Accordingly, with full consideration of the statistical data and satellite measurements [51], we assume a 30% increase in NO<sub>x</sub> emissions from thermal power plants during severe heatwaves. We estimate that the total  $NO_x$  emissions could increase by 8.1% and 5.7%, respectively, in the YR region during the persistent heatwaves of 2013 and 2022 (Fig. 2b). Given the vigorous convection and higher boundary layer that would facilitate the diffusion of emitted precursors, the higher ambient NO<sub>x</sub> and isoprene concentrations observed at SORPES (Fig. 2b) further underscore that both human and biogenic emissions have increased during heatwaves.

# 3.3. Mechanisms for aggravated ozone pollution during persistent heatwaves

Observed temperature and ozone anomalies for two persistent heatwave events in July 22–August 15 of 2013 and August 1–22 of 2022 indicate abnormally high ozone levels and sustained high

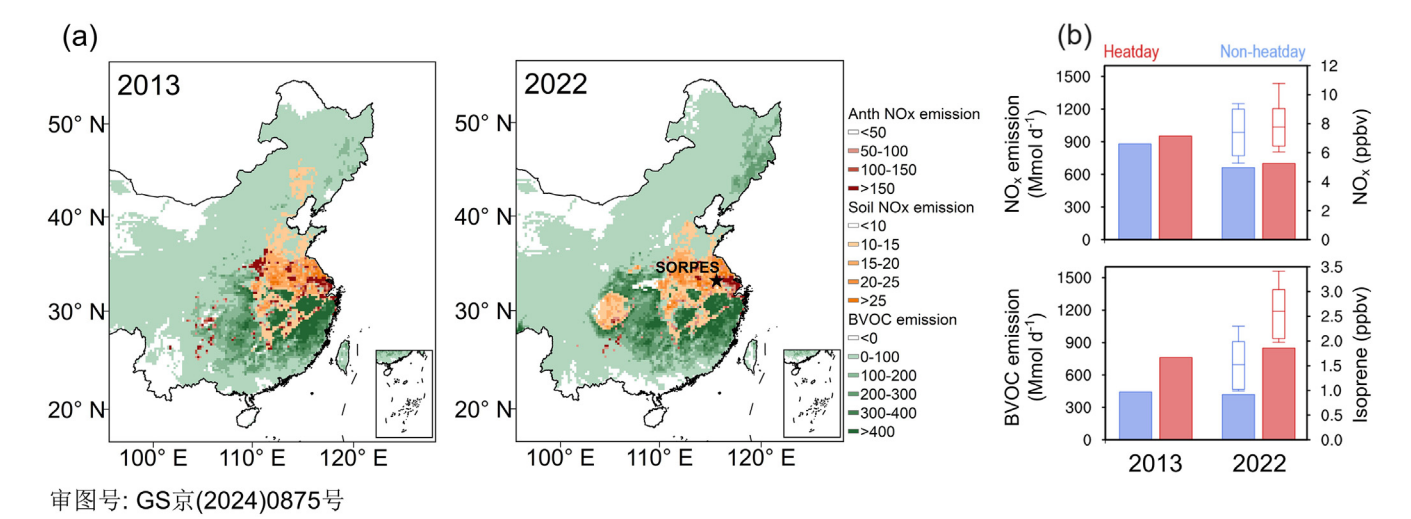


Fig. 2. Heatwave-boosted anthropogenic and biogenic emissions in China. (a) Simulated increases in anthropogenic  $NO_x$ , soil  $NO_x$  and BVOC emissions ( $\times 10^3$  mol d<sup>-1</sup>) in China during the persistent heatwaves compared with non-heatdays in 2013 and 2022. (b) Simulated increases in total anthropogenic  $NO_x$  and BVOC emissions in the YR region on heatdays and non-heatdays during June–August in 2013 and 2022. Statistical concentration ranges (median, upper, and lower tertiles, and upper and lower quartiles) for the daily average  $NO_x$  and daily maximum isoprene concentrations observed at SORPES are also depicted as box charts in (b).

temperatures (typically more than 3–5°C above seasonal averages) in the YR region (Fig. S9 online). To comprehensively understand the roles of atmospheric physical and chemical processes, as well as human-natural systems interactions in heat-stressed O<sub>3</sub> pollution, we conducted multiple WRF/Chem meteorology-chemistry parallel simulations with process diagnosis. The WRF/Chem model effectively captures the spatial distribution and magnitude of observed ground-level ozone hotspots during the two regional heatwaves (Fig. S10 online). High air temperatures and other associated weather conditions on heatdays, such as strong solar radiation and low atmospheric humidity (Fig. S11 online), directly promote the photochemical production of O<sub>3</sub> within the boundary layer (8.5 and 1.7 mg m $^{-2}$  in the 2013 and 2022 heatwaves) and indirectly increase the anthropogenic and biogenic emissions of ozone precursors (15.3 and 13.6 mg  $m^{-2}$  for the 2013 and 2022 heatwaves; Fig. 3c, d). This leads to a significantly enhanced daytime ozone chemical mass within the boundary layer over the severely affected heatwave areas (Fig. 3a, b). Particularly, the significantly increased BVOC and soil NO<sub>x</sub> emissions during hot summers lead to considerably higher surface O<sub>3</sub> levels exceeding 30  $\mu g\ m^{-3}$  from northern to mid-eastern China (Fig. S12a, b online). The chemical contribution of biogenic emissions to daytime O<sub>3</sub> production could increase to more than 30% in the YRD urban agglomeration during the two persistent heatwaves, which is approximately 50% higher than that on non-heatdays (Fig. 3c, d). Additionally, heat-boosted biogenic emissions also dramatically increase the ozone-temperature sensitivity (m) and reduce the discrepancies between the model and observations (Fig. S13 online). For instance, an increase in surface ozone with rising air temperature from 20 to 40  $^{\circ}$ C can reach up to 50  $\mu g \ m^{-3}$  due to faster chemical reaction rates, while enhanced biogenic emissions can add an additional 50–80  $\mu g$  m<sup>-3</sup>. The assumed increase in power plant NO<sub>x</sub> emissions could either worsen or alleviate regional ozone pollution during heatwaves, but with a much smaller impact of less than 5  $\mu g \, m^{-3}$  (Fig. S12 online). Model calculations [52] and observations [53] have shown that since the implementation of clean air actions, the ozone chemical regime in Chinese cities has shifted towards NO<sub>x</sub>-limited or transitional regimes. The distinct responses of O<sub>3</sub> to heat-boosted NO<sub>x</sub> emissions from power sectors in the city centers of YRD may be influenced by the varying O<sub>3</sub> chemical regimes between 2013 and 2022.

In addition, atmospheric physical processes are also responsible for the build-up or dissipation of ozone during heatwaves. Positive ozone anomalies during heatwaves are significantly reduced by the northward horizontal transport (-9.4 and -5.1 mg m<sup>-2</sup> for the 2013 and 2022 heatwaves; see Fig. 3c, d) due to the presence of a stable West-Pacific high-pressure system. Also, the deeper mixing layer and large-scale vertical convection (Fig. S11 online) induced by strong thermal buoyancy during heatwaves could entrain the high-O<sub>3</sub> air mass upward, reducing the O<sub>3</sub> mass within the atmospheric boundary layer (-5.2 and -7.8 mg m<sup>-2</sup> for the 2013 and 2022 heatwaves; Fig. 3c, d). Even more importantly, it is noted that dry deposition could explain more than 20% of the O<sub>3</sub> loss in the atmosphere, and the daytime ozone removal through dry deposition is greatly suppressed during heatwaves (Fig. S14 online). For example, the modelled daytime-average ozone dry deposition velocity decreases by approximately 0.1 cm s<sup>-1</sup> on heatwave days over the YRD urban cluster, representing an average reduction of 2%-13% in O<sub>3</sub> removal through dry deposition compared to non-heatdays (Fig. 3c, d). In densely vegetated regions (e.g., mid-eastern and southern China) where plant stomatal uptake may be an important pathway for O<sub>3</sub> deposition, the suppressed dry deposition during heatwaves may contribute comparably to the enhanced O<sub>3</sub> chemical production (Fig. 3a, b). The lower ozone dry deposition may be attributed to the substantially increased vegetation canopy stomatal resistance and, consequently, reduced stomatal uptake of O<sub>3</sub> by water-stressed vegetation linked to the extreme heat and drought (Fig. S14 online), as reported in Europe [17] and America [54]. The suppression of ozone dry deposition, combined with enhanced ozone chemical formation result in an increase in the accumulated O<sub>3</sub> mass within the boundary layer by more than 30% over the highly polluted YRD urban agglomeration during the record-hot summers of 2013 and 2022.

# 3.4. Implications for mitigating concurrent heat and ozone extremes in future climate

As demonstrated above, heat extremes could significantly enhance the chemical production of  $O_3$  through increased emissions and accelerated chemical reaction rates. However, it is noteworthy that the ozone responses stimulated by heat are highly

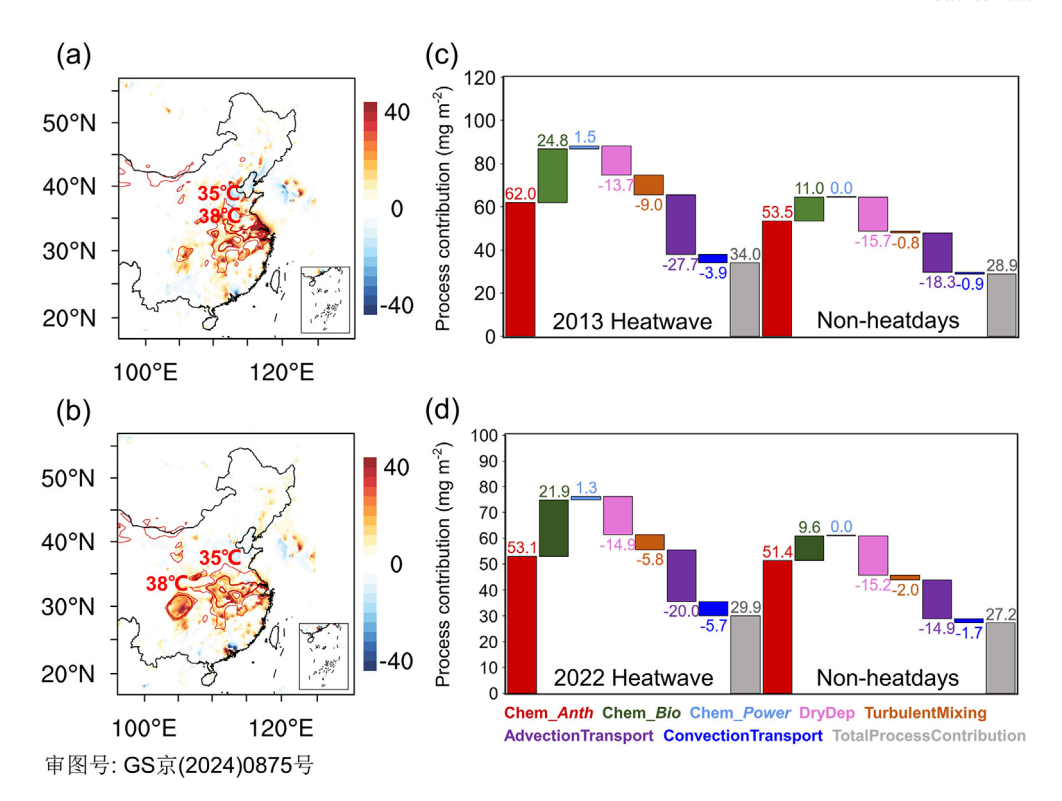


**Fig. 3.** Physical and chemical interactions exacerbate ozone pollution within the boundary layer during the persistent heatwaves in 2013 (upper panels) and 2022 (bottom panels). (a, b) Enhanced chemical production of daytime ozone (mg m<sup>-2</sup>) at 12:00–16:00 local time during the 2013 and 2022 heatwaves. Two contour lines representing daily maximum air temperatures at 35 °C and 38 °C are also indicated. (c, d) Diagnostic process contributions to daytime O<sub>3</sub> concentrations in the YRD during two heatwaves and non-heatdays. Chem\_*Anth*, Chem\_*Bio*, and Chem\_*Power* represent the chemical production of O<sub>3</sub> from anthropogenic sources, biogenic sources, and power plant emissions, respectively; DryDep, TurbulentMixing, AdvectionTransport, and ConvectionTransport represent the removal of O<sub>3</sub> through dry deposition, turbulent mixing, advection, and convection transport, respectively; TotalPocessContribution represents the accumulation of O<sub>3</sub> through the above chemical and physical processes.

dependent on the ambient NO<sub>x</sub>/VOC ratios [6,18]. Using a photochemical box model, we calculated the theoretical isopleth of ozone mixing ratio as a function of varying NO<sub>x</sub> and VOC concentrations, as well as air temperature (Fig. 4 and Fig. S15 online). By examining the relationship between O<sub>3</sub>, NO<sub>x</sub>, VOC and temperature, we discover that the sensitivity of  $O_3$  to temperature varies significantly depending on the emission conditions. The O<sub>3</sub>-NO<sub>x</sub>temperature isopleth appears to be nonlinear and can be divided into low-NO<sub>x</sub> regime, maximal-O<sub>3</sub> regime, and high-NO<sub>x</sub> regime. Under a high- $NO_x$  regime (e.g., typically > 20 ppbv), the ozone mixing ratio increases rapidly with temperature. The maximal ozone production tends to peak at high temperatures and moderate NO<sub>x</sub> levels (i.e., in the maximal-O<sub>3</sub> regime). Under a low-NO<sub>x</sub> regime, the minimal amount of ozone is produced, and the formation of ozone is significantly less affected by temperature over a wide temperature range. The box model also takes into account the additional influence of temperature-dependent isoprene emission on the O<sub>3</sub>-NO<sub>x</sub>-temperature relationship. A twofold increase in the initial isoprene concentration is predicted between 31 and 41°C (Fig. S15b online). The temperature-dependent emission of biogenic VOC increases the sensitivity of ozone pollution to high air temperatures. As a result, a peak O<sub>3</sub> mixing ratio two-thirds higher is produced compared with that caused by faster chemical reaction rates. In terms of the O<sub>3</sub>-VOC-temperature relationship (Fig. S15a online), we find that the ozone concentration and its temperature sensitivity are more influenced by VOC emissions. A decrease in VOC emissions would effectively alleviate O<sub>3</sub> pollution and its sensitivity to temperature.

These nonlinear relationships between  $O_3$ ,  $NO_x$ , VOC, and temperature are consistent with those determined by Coates et al. [6] and Pusede et al. [18] using an analytical model constrained to observations in California. The larger  $O_3$  increases in the

maximal-O<sub>3</sub> and high-NO<sub>x</sub> regimes indicate that significant reductions in NO<sub>x</sub> emissions are necessary to counteract the O<sub>3</sub> increase at high temperatures. Since the implementation of China's clean air actions in 2013, strict emission control has led to a remarkable reduction in NO<sub>x</sub> mixing ratio from 19.7 to 12.7 ppbv (a decrease of 35.5%; Fig. 4b), while VOC levels in the YRD urban agglomeration remained relatively stable [22]. This change may have transitioned the region into a low-NO<sub>x</sub> regime, resulting in reduced ozonetemperature sensitivity. But it should be noted that the idealized simulations do not account for the potentially larger increase in O<sub>3</sub> at high temperatures due to additional anthropogenic sources. In addition to emissions, the relationship between O<sub>3</sub> and temperature may also be influenced by other environmental factors, such as the temperature-dependent curve of water vapor content [55]. Further assessment of these complex influences would be beneficial in order to reduce O<sub>3</sub> pollution in urban areas.

Summer heatwaves are expected to become increasingly intense and frequent [56]. Understanding how and to what extent these future compound extremes respond to human activities is of great importance in mitigating the extreme events and their associated impacts in Chinese cities. We obtained the GCM forecasts of air temperature and NO<sub>x</sub> concentrations in the YRD urban agglomeration under five scenarios. Inter-comparisons of these scenarios show consistent warming trends by the end of this century (0.20-5.46 °C), whereas much stronger warming is projected for the SSP370 and SSP585 scenarios with middle-to-high radiative forcing (Fig. S16 online). Wang et al. [24] also reported an increased risk of heat extremes in China for the next century, with every 1 °C warming translating into an additional ten extreme heat events. Based on the O<sub>3</sub>-NO<sub>x</sub>-temperature isopleth and CMIP6 ensemble forecasts, the SSP370 scenario is expected to fall into the high-NO<sub>x</sub> regime and easily trigger frequent co-occurrence of

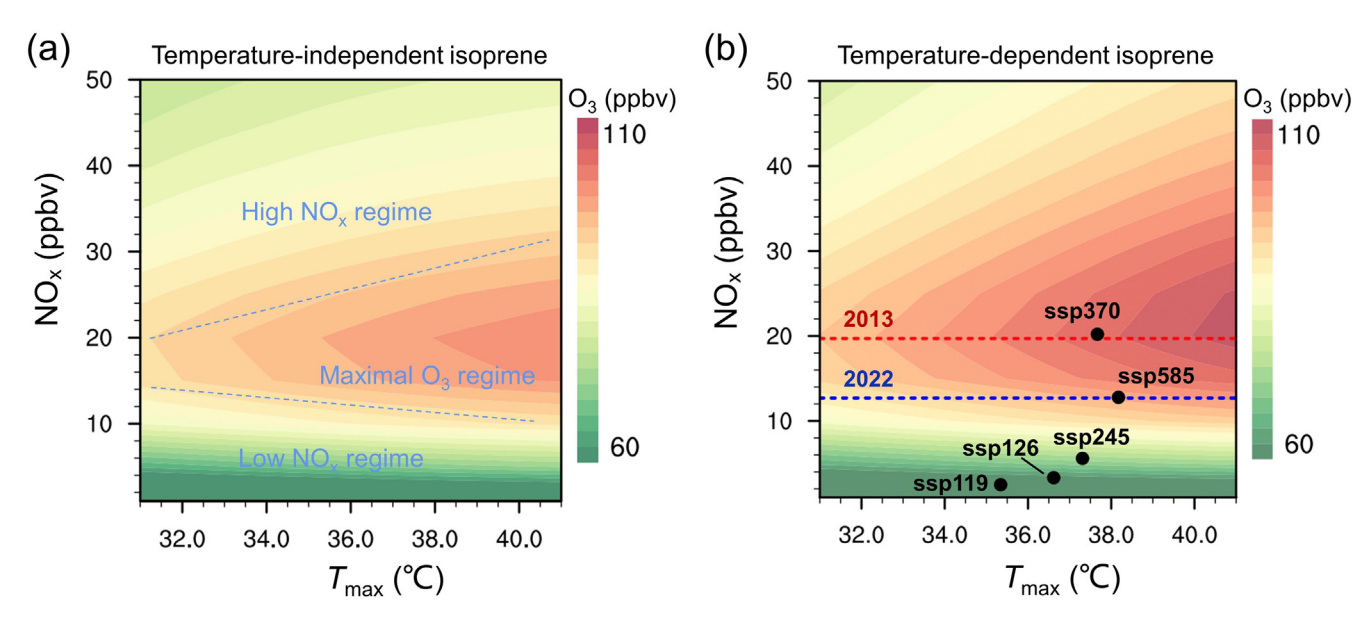


**Fig. 4.**  $O_3$ -temperature relationships under varying  $NO_x$  conditions calculated by the photochemical box model. (a, b) Isopleth of  $O_3$  mixing ratio as a function of  $NO_x$  concentration and temperature with temperature-independent and temperature-dependent isoprene emissions. Two dashed lines in (b) represent the modelled average  $NO_x$  concentrations in the YRD urban agglomeration for the summers of 2013 and 2022. The black dots represent the projected  $NO_x$  concentration and daily maximum air temperature in the mid-term period (2055–2074) under different CMIP6 climate-emission scenarios.

heat and ozone extremes (Fig. 4b). A synergistic clean air and climate mitigation policy will yield significant environmental and climatic co-benefits. It is worth noting that China has announced its ambitious climate commitment to peak carbon emissions before 2030 and achieve carbon neutrality before 2060 by transitioning from fossil fuel-driven energy to low-carbon energy sources. In light of the numerous shared anthropogenic sources of greenhouse gases and air pollutants, such a transition to low-carbon energy pathway is expected to result in significant improvements in air quality in China [57,58] and greatly enhance the sustainability of rapidly expanding urban areas.

# 4. Discussion and conclusions

Under a global warming climate and accelerated urbanization, humans are facing the most challenging climate and environmental crises in the Anthropocene, in which concurrent heatwaves and ozone extremes have led to the most disastrous threats. This study demonstrates a nearly tripled increase in heatwave frequency and intensity in China since the beginning of this century. These heatwaves are increasingly concentrated in the densely populated metropolitan areas of mid-eastern China, coinciding with severe ozone pollution. Evidence from field measurements, satellite retrievals, and model results all confirm the significant increase in human and biogenic emissions during heatwaves. The heatboosted emissions and suppressed dry deposition in the extremely hot and dry summers of 2013 and 2022 exacerbated the ozone pollution within the boundary layer by more than 30% in China's urban agglomerations.

Model calculations demonstrate that the sensitivity of ozone to heat is significantly influenced by emissions from human activities. China's clean air initiatives over the past decade have altered the relationship between ozone and temperature in urban areas. The CMIP6 GCMs predict that energy-intensive and high-emission scenarios are likely to exacerbate the co-occurrence of heatwaves and ozone extremes. This poses a great challenge to human well-being in Chinese megacities and other developing regions. Developing a synergistic clean air and climate mitigation strategy is expected to offer significant environmental and climatic co-benefits to sustainable urban development.

Our findings highlight the great importance of comprehending the comprehensive mechanism and implementing a mitigation strategy for concurrent heatwaves and ozone extremes. Furthermore, there is increasing evidence that urbanization could significantly increase the risk of extreme heat in cities (20%–40%), similar to the warming effect of greenhouse gases [24]. Now, more than half of the global population resides in cities, and it is projected to increase to 6.7 billion (68.4% of the total population) by 2050 (https://population.un.org/wup/). The expanded urbanization and human emissions will intensify the frequency of urban extreme heat events in China by two to five times by the end of this century [24]. Given the complex interactions between climate extremes and urban air pollution, it is crucial to understand the impacts of city expansion on combined heat and ozone extremes. Additionally, exploring potential mitigation strategies is essential to address the dual challenge of urban sustainability.

## **Conflict of interest**

The authors declare that they have no conflict of interest.

# Acknowledgment

This study is supported by the National Key Basic Research Development Program of China (2022YFC3701105), and the National Natural Science Foundation of China (42293322 and 42275100).

### **Author contributions**

Mengmeng Li conducted the majority of the data analyses and model simulations, and also wrote and revised the manuscript. Xin Huang conceived and supervised the manuscript. Shiyi Lai conducted the box model simulations. Dan Yan, Zihan Zhang, and Lei Zhu participated in the data acquisition and statistical analysis of the manuscript. Yuting Lu, Xinyi Jiang, and Nan Wang participated in the model simulations and analyses for this manuscript. Tijian Wang, Yu Song, and Aijun Ding assisted in supervising the manuscript.

# Appendix A. Supplementary materials

Supplementary materials to this article can be found online at https://doi.org/10.1016/i.scib.2024.05.034.

#### References

- [1] Perkins-Kirkpatrick SE, Lewis SC. Increasing trends in regional heatwaves. Nat Commun 2020;11:1–8.
- [2] Hondula DM, Davis RE. The predictability of high-risk zones for heat-related mortality in seven US cities. Nat Hazards 2014;74:771–88.
- [3] Cristofanelli P, Bonasoni P, Carboni G, et al. Anomalous high ozone concentrations recorded at a high mountain station in Italy in summer 2003. Atmos Environ 2007;41:1383–94.
- [4] Gao M, Wang F, Ding Y, et al. Large-scale climate patterns offer preseasonal hints on the co-occurrence of heat wave and O<sub>3</sub> pollution in China. Proc Natl Acad Sci USA 2023:120:1–9.
- [5] Schwarz L, Hansen K, Alari A, et al. Spatial variation in the joint effect of extreme heat events and ozone on respiratory hospitalizations in California. Proc Natl Acad Sci USA 2021;118:1–9.
- [6] Coates J, Mar KA, Ojha N, et al. The influence of temperature on ozone production under varying NO<sub>x</sub> conditions—A modelling study. Atmos Chem Phys 2016;16:11601–15.
- [7] Steiner AL, Davis AJ, Sillman S, et al. Observed suppression of ozone formation at extremely high temperatures due to chemical and biophysical feedbacks. Proc Natl Acad Sci USA 2010;107:19685–90.
- [8] Bloomer BJ, Stehr JW, Piety CA, et al. Observed relationships of ozone air pollution with temperature and emissions. Geophys Res Lett 2009;36:1–5.
- [9] Pu X, Wang TJ, Huang X, et al. Enhanced surface ozone during the heat wave of 2013 in Yangtze River Delta region. China Sci Total Environ 2017;603-604:807-16.
- [10] Kou WB, Gao Y, Zhang SQ, et al. High downward surface solar radiation conducive to ozone pollution more frequent under global warming. Sci Bull 2023;68:388–92.
- [11] Wang N, Huang X, Xu JW, et al. Typhoon-boosted biogenic emission aggravates cross-regional ozone pollution in China. Sci Adv 2022;8:1–8.
- [12] Churkina G, Kuik F, Bonn B, et al. Effect of VOC emissions from vegetation on air quality in Berlin during a heatwave. Environ Sci Technol 2017;51:6120–30.
- [13] Ma MC, Gao Y, Wang YH, et al. Substantial ozone enhancement over the North China Plain from increased biogenic emissions due to heat waves and land cover in summer 2017. Atmos Chem Phys 2019;19:12195–207.
- [14] Wang H, Lu XC, Seco R, et al. Modeling isoprene emission response to drought and heatwaves within MEGAN using evapotranspiration data and by coupling with the Community Land Model. J Adv Model Earth Sy 2022;14:1–22.
- [15] Solberg S, Hov O, Sovde A, et al. European surface ozone in the extreme summer 2003. J Geophys Res-Atmos 2008;113:1–16.
- [16] Ning GC, Wardle DA, Yim SHL. Suppression of ozone formation at high temperature in China: From historical observations to future projections. Geophys Res Lett 2022;49:1–10.
- [17] Lin MY, Horowitz LW, Xie YY, et al. Vegetation feedbacks during drought exacerbate ozone air pollution extremes in Europe. Nat Clim Change 2020;10:444–51.
- [18] Pusede SE, Gentner DR, Wooldridge PJ, et al. On the temperature dependence of organic reactivity, nitrogen oxides, ozone production, and the impact of emission controls in San Joaquin Valley, California. Atmos Chem Phys 2014;14:3373–95.
- [19] Jiang Z, Zhu R, Miyazaki K, et al. Decadal variabilities in tropospheric nitrogen oxides over United States, Europe, and China. J Geophys Res-Atmos 2022;127:1–15.
- [20] Huang J, Yuan ZB, Duan YS, et al. Quantification of temperature dependence of vehicle evaporative volatile organic compound emissions from different fuel types in China. Sci Total Environ 2022;813:1–9.
- [21] China Meteorological Administration. China Bluebook for Climate Change. Beijing: China Meteorological New Press; 2022.
- [22] Lu X, Zhang L, Wang XL, et al. Rapid increases in warm-season surface ozone and resulting health impact in China since 2013. Environ Sci Tech Let 2020;7:240-7.
- [23] Lu KD, Zhou HH, Lee JM, et al. Ozone mitigations beyond the control of nitrogen oxides and volatile organic compounds. Sci Bull 2023;68:1989–92.
- [24] Wang J, Chen Y, Liao WL, et al. Anthropogenic emissions and urbanization increase risk of compound hot extremes in cities. Nat Clim Change 2021;11:1084–9.
- [25] Hersbach H, Bell B, Berrisford P, et al. The ERA5 global reanalysis. Q J R Meteor Soc 2020;146:1999–2049.
- [26] De Smedt I, Theys N, Yu H, et al. Algorithm theoretical baseline for formaldehyde retrievals from S5P TROPOMI and from the QA4ECV project. Atmos Meas Tech 2018;11:2395–426.
- [27] Ding AJ, Fu CB, Yang XQ, et al. Ozone and fine particle in the western Yangtze River Delta: An overview of 1 yr data at the SORPES station. Atmos Chem Phys 2013;13:5813–30.

[28] Fischer EM, Schar C. Consistent geographical patterns of changes in high-impact European heatwaves. Nat Geosci 2010;3:398–403.

- [29] Grell GA, McKeen S, Michalakes J, et al. Real-time simultaneous prediction of air pollution and weather during the Houston 2000 field experiment. In: Fourth Conference on Atmospheric Chemistry: Urban, Regional and Global Scale Impacts of Air Pollutants, 2002. p. 224–7.
- [30] Niu GY, Yang ZL, Mitchell KE, et al. The community Noah land surface model with multiparameterization options (Noah-MP): 1. Model description and evaluation with local-scale measurements. J Geophys Res-Atmos 2011:116:1–19.
- [31] Zaveri RA, Peters LK. A new lumped structure photochemical mechanism for large-scale applications. J Geophys Res-Atmos 1999;104:30387–415.
- [32] Guenther A, Karl T, Harley P, et al. Estimates of global terrestrial isoprene emissions using MEGAN (Model of Emissions of Gases and Aerosols from Nature). Atmos Chem Phys 2006;6:3181–210.
- [33] Sakulyanontvittaya T, Duhl T, Wiedinmyer C, et al. Monoterpene and sesquiterpene emission estimates for the United States. Environ Sci Technol 2008;42:1623–9.
- [34] Williams EJ, Hutchinson GL, Fehsenfeld FC. NO<sub>x</sub> and N<sub>2</sub>O emissions from soil. Global Biogeochem Cy 1992;6:351–88.
- [35] Wesely ML. Parameterization of surface resistances to gaseous dry deposition in regional-scale numerical-models. Atmos Environ 1989;23:1293–304.
- [36] Jin ZP, Yan D, Zhang ZH, et al. Effects of elevated ozone exposure on regional meteorology and air quality in China through ozone-vegetation coupling. J Geophys Res-Atmos 2023;128:1–19.
- [37] Mozaffar A, Zhang YL. Atmospheric volatile organic compounds (VOCs) in China: A review. Curr Pollut Rep 2020;6:250–63.
- [38] Mukherjee S, Mishra AK. Increase in compound drought and heatwaves in a warming world. Geophys Res Lett 2021;48:1–13.
- [39] Gu SH, Huang CR, Bai L, et al. Heat-related illness in China, summer of 2013. Int J Biometeorol 2016;60:131–7.
- [40] Barreira LMF, Duporte G, Ronkko T, et al. Field measurements of biogenic volatile organic compounds in the atmosphere using solid-phase microextraction arrow. Atmos Meas Tech 2018;11:881–93.
- [41] Kleist E, Mentel TF, Andres S, et al. Irreversible impacts of heat on the emissions of monoterpenes, sesquiterpenes, phenolic BVOC and green leaf volatiles from several tree species. Biogeosciences 2012;9:5111–23.
- [42] Opacka B, Muller JF, Stavrakou T, et al. Global and regional impacts of land cover changes on isoprene emissions derived from spaceborne data and the MEGAN model. Atmos Chem Phys 2021;21:8413–36.
- [43] Stavrakou T, Mueller JF, Bauwens M, et al. Impact of short-term climate variability on volatile organic compounds emissions assessed using OMI satellite formaldehyde observations. Geophys Res Lett 2018;45:8681–9.
- [44] Wang P, Schade G, Estes M, et al. Improved MEGAN predictions of biogenic isoprene in the contiguous United States. Atmos Environ 2017;148:337–51.
- [45] Warneke C, de Gouw JA, Del Negro L, et al. Biogenic emission measurement and inventories determination of biogenic emissions in the eastern United States and Texas and comparison with biogenic emission inventories. J Geophys Res-Atmos 2010;115:1–21.
- [46] Harkey M, Holloway T, Kim EJ, et al. Satellite formaldehyde to support model evaluation. J Geophys Res-Atmos 2021;126:1–18.
- [47] Lu X, Ye XP, Zhou M, et al. The underappreciated role of agricultural soil nitrogen oxide emissions in ozone pollution regulation in North China. Nat Commun 2021;12:1–9.
- [48] Oikawa PY, Ge C, Wang J, et al. Unusually high soil nitrogen oxide emissions influence air quality in a high-temperature agricultural region. Nat Commun 2015;6:1–10.
- [49] Lee JD, Lewis AC, Monks PS, et al. Ozone photochemistry and elevated isoprene during the UK heatwave of August 2003. Atmos Environ 2006;40:7598–613.
- [50] Rubin JI, Kean AJ, Harley RA, et al. Temperature dependence of volatile organic compound evaporative emissions from motor vehicles. J Geophys Res-Atmos 2006;111:1-7.
- [51] Liu S, Shu L, Zhu L, et al. Underappreciated emission spikes from power plants during heatwaves observed from space: Case studies in India and China. Earth's Future 2024;12:1–15.
- [52] Yan D, Jin Z, Zhou Y, et al. Anthropogenically and meteorologically modulated summertime ozone trends and their health implications since China's clean air actions. Environ Pollut 2024:1–11.
- [53] Wang WN, Ronald V, Ding JY, et al. Spatial and temporal changes of the ozone sensitivity in China based on satellite and ground-based observations. Atmos Chem Phys 2021;21:7253–69.
- [54] Huang L, McDonald-Buller EC, McGaughey G, et al. The impact of drought on ozone dry deposition over eastern Texas. Atmos Environ 2016;127:176–86.
- [55] Zhang JX, Gao Y, Leung LR, et al. Disentangling the mechanism of temperature and water vapor modulation on ozone under a warming climate. Environ Res Lett 2022;17:1–12.
- [56] Meehl GA, Tebaldi C. More intense, more frequent, and longer lasting heat waves in the 21st century. Science 2004;305:994–7.
- [57] Cheng J, Tong D, Zhang Q, et al. Pathways of China's PM<sub>2.5</sub> air quality 2015–2060 in the context of carbon neutrality. Natl Sci Rev 2021;8:1–11.
- [58] Tang R, Zhao J, Liu YF, et al. Air quality and health co-benefits of China's carbon dioxide emissions peaking before 2030. Nat Commun 2022;13:1–9.



Mengmeng Li received her Ph.D. degree from Peking University in 2015. She is presently an associate professor at School of Atmospheric Sciences, Nanjing University. Her research interest focuses on the atmospheric chemistry, urban meteorology and air pollution, and interactions between extreme weather and air quality.



Xin Huang, Ph.D., a professor at School of Atmospheric Sciences, Nanjing University. Her research interest focuses on air pollution and its interaction with meteorology in highly polluted regions like China.